Design of terahertz reconfigurable devices by locally controlling topological phases of square gyro-electric rod arrays

Zhang, L.; Xiao, Sanshui

Published in:
Optical Materials Express

Link to article, DOI:
10.1364/OME.9.000544

Publication date:
2019

Document Version
Publisher's PDF, also known as Version of record

Research Article | Vol. 9, No. 2 | 1 Feb 2019 | OPTICAL MATERIALS EXPRESS 544

Optical Materials EXPRESS

Design of terahertz reconfigurable devices by locally controlling topological phases of square gyro-electric rod arrays

L. ZHANG[1,2] AND SANSHUI XIAO[2,*]

[1]*Key Laboratory of Electromagnetic Wave Information Technology and Metrology of Zhejiang Province, College of Information Engineering, China Jiliang University, Hangzhou 310018, China*
[2]*DTU Fotonik, Department of Photonics Engineering, Technical University of Denmark, Kongens Lyngby, DK-2800, Denmark*
**saxi@fotonik.dtu.dk*

Abstract: In topological photonics, there is a class of designing approaches that usually tunes topological phase from trivial to non-trivial in a magneto-optical photonic crystal by applying an external magnetic field to break time reversal symmetry. Here we theoretically realize topological phase transition by rotating square gyro-electric rods with broken time reversal symmetry. By calculating band structures and Chern numbers, in a simple square-lattice photonic crystal, we demonstrate the topological phase transition at a specific orientation angle of the rods. Based on the dependence of topological phase on the orientation angle, we propose several terahertz devices including an isolator, circulator and splitter in a 50x50 reconfigurable rod array by locally controlling topological phases of the rods. These results may have potential applications in producing reconfigurable terahertz topological devices.

1. Introduction

Photonic topological insulator (PTI) in a photonic system is an analogue of electronic topological insulator in an electronic system [1–3]. It can support topologically protected defect-immune edge state thus draws much attention. According to the process of development, there are several PTIs realized by different methods [4–19]. They can be divided into two classes. One class breaks time reversal symmetry while the other keeps time reversal invariant. In the first class, the simplest way to break time reversal symmetry is to apply an external magnetic field. This kind of PTI was first proposed in photonic crystal by Raghu and Haldane with photonic quantum anomalous Hall (QAH) effect [4,5] and then experimentally demonstrated in magneto-optical photonic crystal composed of gyro-magnetic materials [6]. More researches on this class keep going in recent years [7–12]. Because the time reversal symmetry of the gyro-magnetic (or gyro-electric) crystal is broken by magnetic field, the topological protected edge waves in this class are strictly non-reciprocal. In the second class with time reversal invariant, PTI can be realized by using different mechanisms. One approach is based on photonic quantum spin Hall (QSH) effect (relying on the symmetry of the electromagnetic field). This kind of PTI have been realized in many systems including bi-anisotropic metacrystals [13] and C6-symmetric all-dielectric photonic crystal [14,15], where two pseudospin states in the photonic system play the same roles of two spin states in the electronic system. Another approach relies on photonic quantum valley Hall (QVH) effect. Several groups have already realized this kind of PTI in all-dielectric photonic crystals [16,17] or bi-anisotropic metamaterials [18] or surface plasmon crystals [19], where valley symmetry is broken and the edge states are valley dependent. Because of invariant time reversal symmetry, the topological protected edge

#352697 https://doi.org/10.1364/OME.9.000544
Journal © 2019 Received 23 Nov 2018; revised 24 Dec 2018; accepted 24 Dec 2018; published 14 Jan 2019

Optical Materials EXPRESS

waves in the second class are reciprocal. The robust edge states exist but only spin or valley polarized state shows unidirectional propagation.

To realize the first class of PTIs with broken time reversal symmetry, usually a large magnetic field in the order of several Teslas is necessary for the gyro-magnetic materials to provide enough magneto-optical response in the optical or microwave band. In past few years, it is found that the cyclotron resonance effect in semiconductor materials (such as InSb) can be used to break time reversal symmetry with a relatively small magnetic field at terahertz (THz) frequencies [20–24]. Thus THz topological devices by using the cyclotron resonance effect in semiconductor materials are proposed [25]. Similar method is used to obtain THz one-way edge propagation in photonic crystal [26]. More topological applications in terahertz band are expected to come out soon.

Relying on the dependence of topological phases on the orientations of the rods, we in this paper design several THz devices including isolator, circulator and splitter in a 50x50 rod array. This array is a square-lattice photonic crystal formed by square rods made of InSb. Under a relatively small magnetic field, we find the topological phase of the photonic crystal transits from trivial to non-trivial at the orientation angle near 33 degree through the calculations of band structures and Chern numbers. By controlling the topological phases of the rods with different orientation, we can manipulate wave propagation and realize different functionalities inside this 50x50 angle-reconfigurable rod array.

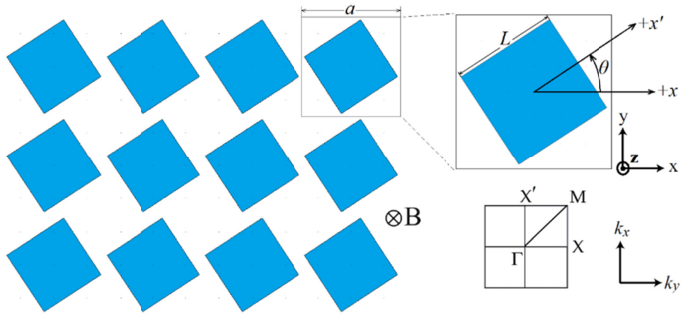

Fig. 1. Schematic of square semiconductor rod array arranged in a square lattice filled with air. In enlarged unit cell, a is the lattice constant, L is the side length of the square rod, θ is the rotated angle from + x to + x' axis presenting the rod orientation. The first Brillouin zone is also square. The magnetic field B is applied along z-axis.

2. Theoretical model and method

The photonic crystal designed in this work consists of square gyro-electric semiconductor rods arranged in a square lattice filled with air, as shown in Fig. 1. The side length of the square rod is L and the lattice constant is a. The + x axis of the square lattice and the + x' axis of the square rod are overlapping at the beginning. When the rod is rotated anticlockwise, there is angle θ between the + x axis and + x' axis as shown in the unit cell. Because of the structural symmetry, we only consider the rotation angle θ from 0° to 45°. The Brillouin zone (BZ) is square and the BZ edges are formed by Γ-X-M-X'-Γ, as shown the inset in Fig. 1. The square rods become gyro-electric anisotropic when an external magnetic field B is applied along rod-length direction (z-axis). The dielectric permittivity tensor can be expressed as [27]

$$\varepsilon = \varepsilon_\infty \begin{bmatrix} \varepsilon_1 & i\varepsilon_2 & 0 \\ -i\varepsilon_2 & \varepsilon_1 & 0 \\ 0 & 0 & \varepsilon_3 \end{bmatrix}, \quad (1)$$

Optical Materials EXPRESS

$$\varepsilon_1 = 1 - \frac{\omega_p^2(\omega + i\gamma)}{\omega[(\omega + i\gamma)^2 - \omega_c^2]},$$
$$\varepsilon_2 = \frac{\omega_p^2 \omega_c}{\omega[(\omega + i\gamma)^2 - \omega_c^2]}, \quad (2)$$
$$\varepsilon_3 = 1 - \frac{\omega_p^2}{\omega(\omega + i\gamma)}$$

where $\omega_c = eB/m^*$ is the electron cyclotron resonance frequency (e is the charge of the electron and m^* is the effective mass of the electron), ω is the angular frequency, γ is the collision frequency of the charge carriers characterizing the material loss, ε_∞ and ω_p is the high frequency limit permittivity and the bulk plasma frequency of the semiconductor respectively. Here we use indium antimonide (InSb) semiconductor to achieve high ω_c under a relatively small magnetic field at THz range. The material parameters of InSb at room temperature are given by $\varepsilon_\infty = 15.68$, $\omega_p = 12.6$ THz, $m^* = 0.014m_0$ (m_0 is the free electron mass in vacuum) [28]. At the working frequency of 3.5 THz in this work, the elements in the permittivity tensor are evaluated as $\varepsilon_1 = 0.585$, $\varepsilon_2 = 0.190$ under $B = 0.8$ T and ε_3 is fixed to be 0.670 no matter how B varies. For simplicity, the material loss is neglected in most of the simulations.

For this kind of semiconductor, only the H-polarized dispersion relation of the bulk modes depends on the cyclotron resonance frequency. To calculate the band structure of the photonic crystal, we solve the Maxwell's equations in the H-field form

$$\nabla \times [\boldsymbol{\varepsilon}^{-1}(\mathbf{r}) \nabla \times \mathbf{H}(\mathbf{r})] = \omega^2 \boldsymbol{\mu}(\mathbf{r}) \mathbf{H}(\mathbf{r}), \quad (3)$$

where $\boldsymbol{\mu}(\mathbf{r})$ and $\boldsymbol{\varepsilon}(\mathbf{r})$ are the permeability and permittivity tensors respectively. ω is the eigenfrequency, which is solved by using the finite-element method in the commercial software COMSOL Multiphysics. The topological properties of the proposed lattice can be explored by calculating Chern number of the nth band (the band with the lowest energy is the 1st band)

$$C_n = (2\pi)^{-1} \int_{BZ} F_{\mathbf{k}}^{(n)} dS_{\mathbf{k}}, \quad (4)$$

where the integral is over the whole BZ and the nth band Berry curvature is expressed as [29]

$$F_{\mathbf{k}}^{(n)} = \nabla_{\mathbf{k}} \times A_{\mathbf{k}}^{(n)} = \nabla_{\mathbf{k}} \times \langle u_{n\mathbf{k}} | \nabla_{\mathbf{k}} | u_{n\mathbf{k}} \rangle, \quad (5)$$

with $A_{\mathbf{k}}^{(n)}$ denoting the Berry connection of the nth band energy $u_{n\mathbf{k}}$. In some cases, when two adjacent bands show mutual degeneracy points, it is better to calculated the composite Chern number of the two bands defined by [30]

$$C_{n\oplus n+1} = (2\pi)^{-1} \int_{BZ} F_{\mathbf{k}}^{(n\oplus n+1)} dS_{\mathbf{k}} = (2\pi)^{-1} \int_{BZ} \mathrm{Tr} \nabla_{\mathbf{k}} \times A_{\mathbf{k}}^{(n\oplus n+1)} dS_{\mathbf{k}}. \quad (6)$$

Here $A_{\mathbf{k}}^{(n\oplus n+1)}$ is 2x2 matrix Berry connection between the nth band energy $u_{n\mathbf{k}}$ and $(n + 1)$th band energy $u_{(n+1)\mathbf{k}}$, and Tr stands for the trace of the matrix. This definition can also be extended to more than two bands with degenerate points. The band and composite Chern numbers are obtained using the method in Ref [31]. Furthermore, the gap Chern number C_g is defined as the sum of the Chern numbers of all the bands below a band gap [10]. This gap Chern number is used to examine the existence of the topological protected edge states between two topologically distinct insulators.

Optical Materials EXPRESS

3. Results and discussion

3.1 Topological band structures

At the beginning, we choose the side length of the square rod $L = 0.68a$ (This choice is explained in the discussion of Sec.3.3). The calculated TE mode ($\mathbf{H} = H_z\mathbf{z}$) band structures of the photonic crystal for two situations at $\theta = 0°$ and $\theta = 45°$ are illustrated in Figs. 2(a) and 2(c) under an external magnetic field $B = 0.8$ T. Under these two rotation angles, the BZ can be reduced to a triangular irreducible BZ along Γ-X-M-Γ. The dispersion shows in Fig. 2(a) a small band gap (presented in green) near $\omega = 0.435$ ($2\pi c/a$) between the 2nd and 3rd bands. Actually, when $B = 0$ T there is a degenerate point shared by the 2nd and 3rd bands at M point, which is not shown here. Therefore, this green gap is opened by breaking the time reversal symmetry that is similar to the method used in many publications presenting QAH phase. In contrast, the blue lines in Fig. 2(c) show when $\theta = 45°$ the gap (presented in cyan) near $\omega = 0.435$ ($2\pi c/a$) between the 2nd and 3rd bands becomes relatively larger. Note that this cyan gap exists when B = 0 T. To explore the topological properties of the bands in the time reversal symmetry broken structure, we calculate the Berry curvature and Chern numbers of the lowest 6 bands. Since there are several degeneracy points between adjacent bands, we directly calculate the composite Chern number instead of individual band Chern numbers, as displayed in red integer numbers in the dash eclipse in Figs. 2(a) and 2(c). It should be mentioned all the band Chern numbers are 0 with time reversal invariant. After breaking the time reversal symmetry, Chern numbers may become nonzero due to the exchange of Berry phase between adjacent bands.

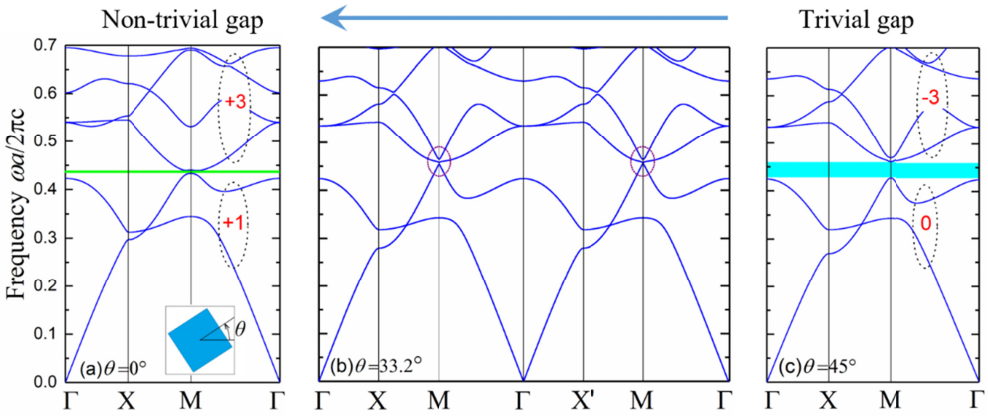

Fig. 2. Band structures of the rod arrays with different rod orientation showing phase transition process. The time reversal symmetry is broken by an external magnetic field B = 0.8 T. The composite Chern numbers are labeled by red integers in the black dash eclipse covering corresponding bands. (a) $\theta = 0°$; The green gap is topologically non-trivial with its gap Chern number $C_g = +1$. (b) $\theta = 33.2°$, the phase transition angle. There is no gap between 2nd and 3rd bands but degenerate points instead as pointed out with purple circles. (c) $\theta = 45°$; The cyan gap is topologically trivial with its gap Chern number $C_g = 0$.

For the case of $\theta = 0°$, the composite Chern number of the lowest two bands below the green gap is + 1 and that of the lowest four bands above the green gap is + 3. Obviously the sum of the Chern numbers of all the bands below the green gap is + 1, which indicates the green gap is topologically non-trivial with its gap Chern number $C_g = +1$. In contrast, for $\theta = 45°$, the composite Chern number of the lowest two bands below the cyan gap is 0 and that of the lowest four bands above the cyan gap is −3. Therefore, the cyan gap in Fig. 2(c) is topologically trivial with $C_g = 0$. This difference is caused by the fact that when the green gap is opened from a degenerate point by the magnetic field, there is exchange of Berry phase

Optical Materials EXPRESS

between lowest two bands and higher bands at the original degenerate point, leading to nonzero composite Chern number of the lowest two bands. On the other hand, the cyan gap already exists without a magnetic field thus is not opened by the broken time reversal symmetry. There is no exchange of Berry phase between the lowest two bands and higher bands, giving rise to zero composite Chern number of the lowest two bands. We can conclude that the photonic crystal with different rod orientation may show different topological phase.

To further explain the topological phase transition process of the lowest band gap with different rod orientation, we calculate the band structures of the cases with other degrees in the range of $0°<\theta<45°$ under the same magnetic field. We find the special case with θ = 33.2°, the transition angle for the topological phase, where its band structure is shown in Fig. 2(b). As pointed out in the purple circle, there are degenerate points between the 2nd and 3rd bands at M and M' points. This degeneracy also occurs without the magnetic field applied. After thorough calculations, we can describe the process of topological phase transition. As indicated by the arrow direction in Fig. 2, if we start from θ = 45°, in the process of clockwise rotating the rods from θ = 45° to θ = 33.2°, the lowest band gap is topologically trivial and becomes narrower until completely closed around θ = 33.2° (reduces to a degenerate point at the transition angle). When we keep rotating the rods from θ = 33.2° to θ = 0°, the lowest band gap is opened up again and maintains during the process. This time the gap turns to be topologically non-trivial, showing the photonic QAH phase.

3.2 Edge states

Robust unidirectional edge states are the most attractive feature which exist at the interface between two insulators with different topological phases. We calculate the projected band diagrams along the edge direction of the photonic crystal with broken time reversal symmetry. In our setting, the photonic crystal consists of an array of the supercell along the x direction. Each supercell (shown in Fig. 3(c)) has 20 unit cells with the same structural size as in Fig. 2 along the y direction. The upper and lower edges are formed by ending the upper and lower boundaries of the supercell with metal plates (set as perfect electric conductor) respectively. The Floquet periodic boundary condition (characterized by the Bloch wavevector k_x) is employed in the x direction. The band diagram for the case of θ = 0° is shown in Fig. 3(a) and the target band gap region is enlarged in Fig. 3(b) for more clear presentation. The lowest white gap region near ω = 0.435 ($2\pi c/a$) agrees with the green gap in Fig. 2(a). Inside the gap, the orange and red lines respectively present the unique edge state on the upper and lower edge. Each edge band locates partially in + k_x region and partially in -k_x region of the band gap, thus the upper and lower edge mode have a crossing in the gap while each edge band connects the bands above and below the gap. The number of edge modes in the band gap is determined by the difference in the gap Chern number of two adjacent insulators [10]. Here in the gap there is one edge mode at a single edge that is in good agreement with its gap Chern number C_g = + 1.

Optical Materials EXPRESS

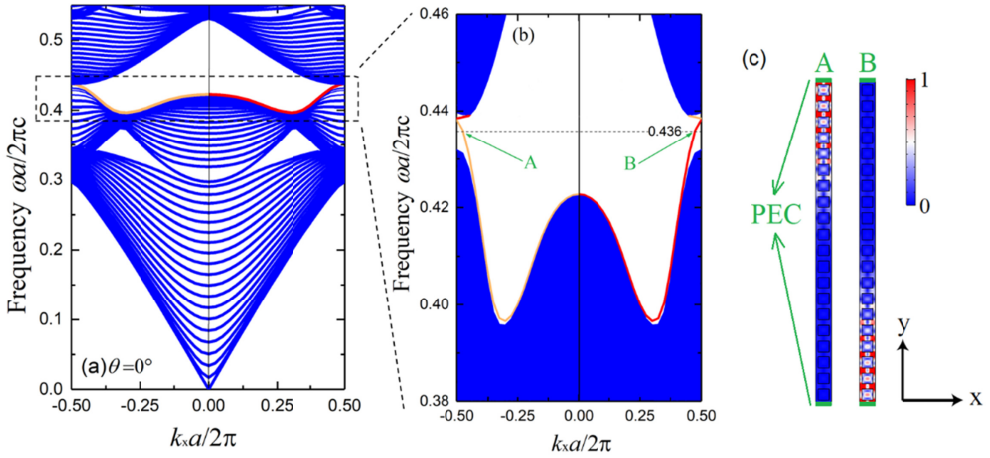

Fig. 3. (a) Projected band diagram of the supercell in $\theta = 0°$ case with upper and lower edges ended by PEC. The blue lines represent bulk projected bands. The red and orange lines inside the gap represent upper and lower edge bands. (b) Enlarged region including the target band gap. A and B are the chosen points of the edge band at $\omega = 0.436$ ($2\pi c/a$). (c) The structure of the supercell and the normalized electric field distribution at the chosen points. The field is confined on the upper edge at A point and on the lower edge at B point.

To demonstrated the edge confinement, we take one point each of upper and lower edge band for examples (labelled with A, B in Fig. 3(b)). At the frequency $\omega = 0.436$ ($2\pi c/a$), the electric fields of A and B in Fig. 3(c) clearly show confined fields on the upper and lower edges respectively. As indicated from the slopes of the band (corresponding to the group velocity), the edge mode A propagates along -x direction while mode B propagates along + x direction. It is illustrated that the fields decay into about five or six rows of the array, mostly due to the small gap. On the other hand, the band diagram for $\theta = 45°$ case is not shown here because there is no edge mode in the lowest band gap with gap Chern number $C_g = 0$.

3.3 Reconfigurable waveguiding

Next, we numerically demonstrate topologically protected THz wave unidirectional propagation along the interface between two regions with different topological phases. In the first presentation, the photonic crystal consists of square rods all with $\theta = 0°$ and lattice constant $a = 37.4\mu m$. With the same external magnetic field, this array has a topological non-trivial band gap. A metal wall is placed under the array (set as PEC) as a topological trivial region and meanwhile reflects THz wave. Another metal slab with width $1a$ and height $5a$ stands on the metal wall as an obstacle to the wave propagation. A magnetic current is put between the photonic crystal and metal wall as a point source to excite THz wave with the frequency $f = 3.5$ THz (equivalent to $\omega = 0.436$ ($2\pi c/a$)). As shown in the electric field distribution in Fig. 4(a), THz wave excited from the source only propagates along + x direction on the lower edge and bypasses the obstacle without blocked. This clearly illustrates the existence of the topologically protected edge mode with its unidirectional and defect-immune properties.

Optical Materials EXPRESS

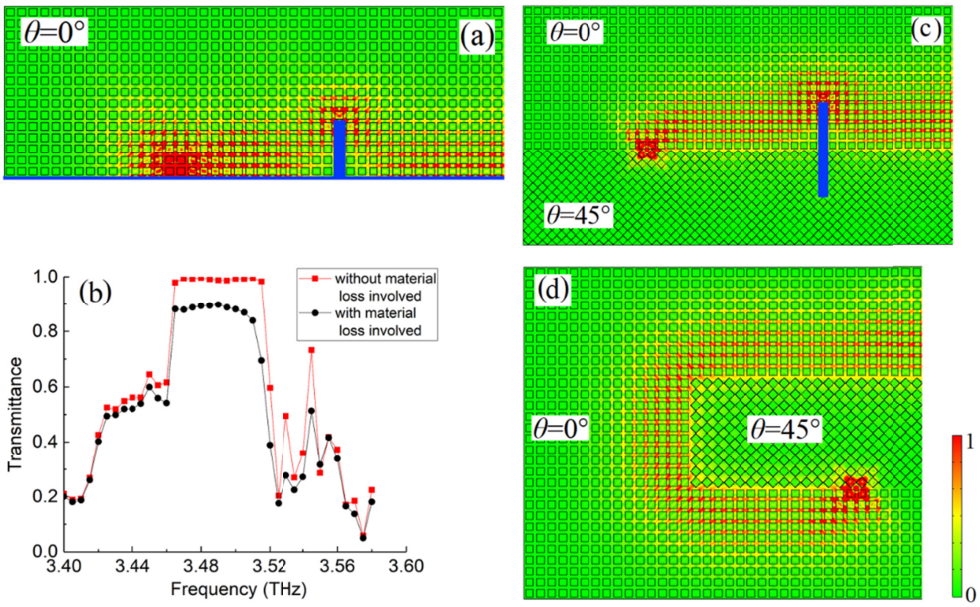

Fig. 4. Normalized electric field distribution of the edge wave propagation. The wave is excited by a point source. Blue areas denote the metal wall and the obstacle. (a) Distribution of edge wave between the array with $\theta = 0°$ and a metal wall at 3.5 THz. (b) Transmission spectrum without and with material loss involved when the wave propagates a length of 30a along the edge. (c) Distribution of edge wave between upper sub array with $\theta = 0°$ and lower sub array with $\theta = 45°$. (d) Distribution of edge wave along the interface with two right-angled bends.

We then evaluate the transmission spectrum near the gap frequencies by integrating the intensity over the cross section of one supercell and over that of another supercell 30a away along the edge. As shown by the red line in Fig. 4(b), the transmittance is nearly unity within the topological transmission band from 3.47 to 3.51 THz after the wave propagating a length of 30a, demonstrating the topologically protected edge waveguiding with almost no loss. At the frequencies outside the band gap of the photonic crystal, the transmittance is not accurately evaluated due to the wave leakage and scattering. For more practical consideration, we examined the influence on the transmission brought by the material loss. Here, $\gamma = 0.001\omega_p$ is taken in Eq. (2) to involve the material loss of InSb. Under the same condition, the transmittance reduces to about 90% in the transmission band as shown by the black line in Fig. 4(b), but the characteristics of the topologically protected transmission do not change much.

Optical Materials EXPRESS

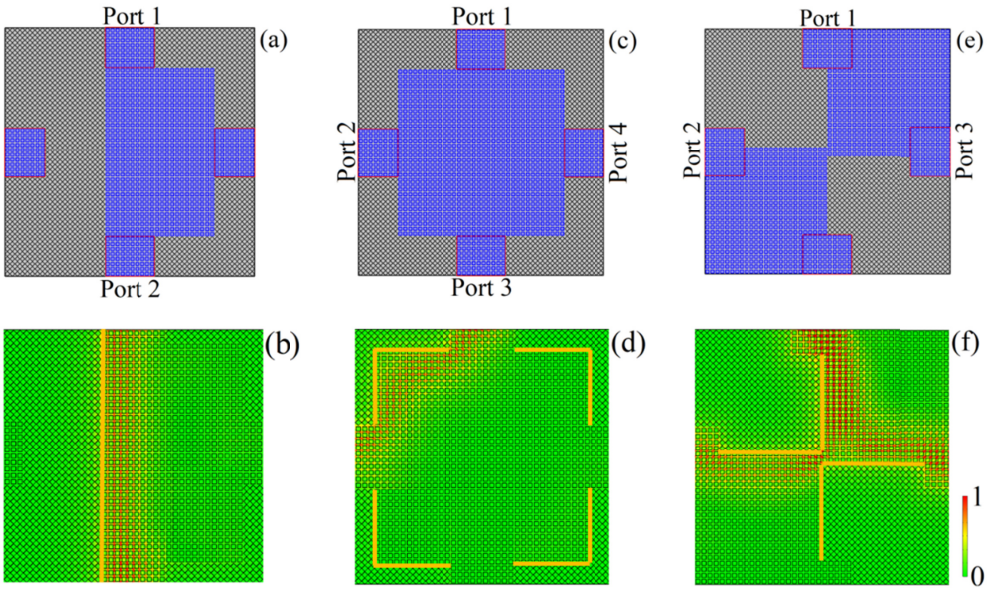

Fig. 5. Reconfigurable square array consists of 50x50 rotatable square rods allowing waves propagating along desired path such as going straight (isolation), going circularly (circulation) and going separately (wave splitting). Blue area is the sub array with $\theta = 0°$ and gray area is the sub array with $\theta = 45°$. Four ports are fix as the uniform interfaces for wave input or output in four red frames. Wave are all input from Port 1 at the frequency of 3.5 THz as an example. Yellow lines in the field plots describe the constructed edges after desired rotating operations. (a-b) 2-port isolation and the waveguiding distribution. (c-d) 4-port circulation and the waveguiding distribution. (e-f) 3-port wave splitting and the waveguiding distribution.

To lay the foundation for designing reconfigurable devices, we present topologically protected edge mode between two arrays. As shown in Fig. 4(c), the rods of the upper sub array are rotated to $\theta = 0°$ and the rods of the lower sub array are rotated to $\theta = 45°$. Because the projected band with this kind of two-array supercell are similar to that in Fig. 3, we do not present it here. The electric field distribution shows one-way defect-immune waveguiding along the interface between two sub arrays, due to the facts that the working frequency of 3.5 THz lies simultaneously inside topologically non-trivial gap of the sub array with $\theta = 0°$ as well as topologically trivial gap of the sub array with $\theta = 45°$. This can be clearly seen by comparing the green gap and cyan gap in Fig. 2. For the topologically trivial cyan gap is much larger than the topologically non-trivial green gap, the edge waves mostly decay a few rows into upper array thus look like locating only above the edge. Here $\theta = 0°$ and $\theta = 45°$ are not necessary for the upper and lower sub arrays. As long as the gaps of two sub arrays with different rod orientation have different topological phases but overlaps, the edge mode will appear at the overlapping frequencies. The robustness of the edge mode also reflects in freely bending propagation. As shown in Fig. 4(d), the rods of an internal sub array are rotated by 45° while all outside rods keep $\theta = 0°$, forming a rectangular interface with two right-angled bends. The waves can turn around the two right-angled corners without any back scattering. Furthermore, it is worth to mention that the side length L of the square rods is not necessary to be $0.68a$ as the first choice in Sec.3.1. We are able to find similar results if the rods have longer L such as $0.69a$ or $0.70a$ (should be shorter than $a/\sqrt{2}$). If L changes, the topological phase transition in the process of rotating rods will no longer take place at $\theta = 33.2°$ but at another nearby angle. However, if the rods take shorter L such as $0.67a$ or less, the working frequencies in upper topologically non-trivial gap may not locate

Optical Materials EXPRESS

inside lower topologically trivial gap at the same time. When working at these frequencies, a large part of the energy will leak away from the lower sub array.

Based on the above examinations, we are now able to control the waveguiding direction by configuring every rotatable rod. So a reconfigurable square array with multipurpose property is proposed for THz applications. This array consists of 50x50 rotatable square rods with the same parameters as in Fig. 4. We fix four ports unchanged as the uniform interfaces for wave input or output as shown in four red frames in Fig. 5(a), (c) and (e). With suitable configuration by rotating every single rod inside the array, this structure can be used for several occasions. Firstly, by rotating left sub array to $\theta = 45°$ and right sub array to $\theta = 0°$ as shown in Fig. 5(a), we can get a 2-port THz isolator to let waves go straight unidirectionally. This isolator allows waves propagating only from Port 1 to Port 2 along the edge of two sub arrays as shown the field distribution at 3.5 THz in Fig. 5(b), while the backward propagating is forbidden. Secondly, by rotating 4 sub arrays near each corner of the whole array to $\theta = 45°$ and all the remaining rods to $\theta = 0°$ as shown in Fig. 5(c), we can obtain a 4-port THz circulator with rotational symmetry to let waves go circularly. When waves input from Port 1, most of the energies propagate along the artificial edge in counterclockwise direction and output from Port 2 but few parts arrive Port 3 and 4, as shown the field distribution at 3.5THz in Fig. 5(d). Because of the circulation property, THz wave can also input from Port 2 or 3 or 4 and will get similar circulated transmission. At last, by rotating the sub arrays in upper left corner as well as lower right corner to $\theta = 45°$ and all the remaining rods to $\theta = 0°$, we can achieve a THz wave splitter to slit waves at the center junction as shown in Fig. 5(e). The waves inputting from Port 1 can split into two edge wave beams at the junction then output from Port 2 and 3 as shown in Fig. 5(f). Here the splitting tunnel is two-row wide at the junction along the y direction, leading to the transmittance of 42.2% at Port 2. The width of the tunnel at the junction will affect the splitting ratio. Obviously, the transmittance at Port 2 becomes lower with narrower junction. For example, if the tunnel is zero-row wide, the transmittance at Port 2 is 16.3%. As mentioned above, the orientations θ in different sub arrays are not necessarily to be 0° or 45°. There are more choices for rod orientations as long as we can make two adjacent sub arrays have different topological phase. In addition, more edge channels can be created by rotating every single rod to make the devices with more ports or guide waves against disorders such as misalignments of the rods along desired path inside the array.

4. Conclusion

We propose a new concept of designing terahertz reconfigurable devices by controlling local topological phases of square-rod photonic crystals. These devices are realized in a 50x50 rod array where the rods are arranged in a square lattice. Magneto-optical semiconductor InSb showing enough gyro-electric response under a relatively small magnetic field is used as the material of the rods. Our calculation results reveal the dependence of the topological phase on the rod orientation. In such a simple photonic crystal, the topological phase transits from trivial to non-trivial at a critical rod angle near 33 degree. The topological non-trivial phase keeps unchanged as long as the orientation of the rods is smaller than the critical angle. The ability of controlling robust wave propagation in the 50x50 domain by changing local topological phases allows us to design terahertz devices with different functionalities. The high isolation ratio of the isolator and circulator is ensured by the non-reciprocal propagations. The splitting ratio of the splitter can also be tuned by adjusting the splitting junction. InSb used in our design is a commercially available and CMOS compatible material, and it can be easily structured, e.g., with a dicing saw [28]. To break the time reversal symmetry, we rely on a relatively small magnetic field lower than 1T, which makes our design feasible for the experimental realization. The concept of locally controlling topological phases paves a new way to realize terahertz reconfigurable devices with new functionality.

Optical Materials EXPRESS

Funding

2018 National Key Research and Development Plan of China (Grant No. 2018YFF01013005).

References

1. L. Lu, J. D. Joannopoulos, and M. Soljačić, "Topological photonics," Nat. Photonics **8**(11), 821–829 (2014).
2. A. B. Khanikaev and G. Shvets, "Two-dimensional topological photonics," Nat. Photonics **11**(12), 763–773 (2017).
3. T. Ozawa, H. M. Price, A. Amo, N. Goldman, M. Hafezi, L. Lu, M. Rechtsman, D. Schuster, J. Simon, O. Zilberberg, and I. Carusotto, "Topological photonics" arXiv:1802.04173(2018).
4. S. Raghu and F. D. M. Haldane, "Analogs of quantum-Hall-effect edge states in photonic crystals," Phys. Rev. A **78**(3), 033834 (2008).
5. F. D. M. Haldane and S. Raghu, "Possible realization of directional optical waveguides in photonic crystals with broken time-reversal symmetry," Phys. Rev. Lett. **100**(1), 013904 (2008).
6. Z. Wang, Y. Chong, J. D. Joannopoulos, and M. Soljacić, "Observation of unidirectional backscattering-immune topological electromagnetic states," Nature **461**(7265), 772–775 (2009).
7. Y. Poo, R. X. Wu, Z. Lin, Y. Yang, and C. T. Chan, "Experimental realization of self-guiding unidirectional electromagnetic edge states," Phys. Rev. Lett. **106**(9), 093903 (2011).
8. K. Liu, L. Shen, and S. He, "One-way edge mode in a gyromagnetic photonic crystal slab," Opt. Lett. **37**(19), 4110–4112 (2012).
9. L. Zhang, D. X. Yang, K. Chen, T. Li, and S. Xia, "Design of nonreciprocal waveguide devices based on two-dimensional magneto-optical photonic crystals," Opt. Laser Technol. **50**(2), 195–201 (2013).
10. S. A. Skirlo, L. Lu, and M. Soljačić, "Multimode One-Way Waveguides of Large Chern Numbers," Phys. Rev. Lett. **113**(11), 113904 (2014).
11. S. A. Skirlo, L. Lu, Y. Igarashi, Q. Yan, J. Joannopoulos, and M. Soljačić, "Experimental observation of large Chern numbers in photonic crystals," Phys. Rev. Lett. **115**(25), 253901 (2015).
12. H. C. Chan and G. Y. Guo, "Tuning topological phase transitions in hexagonal photonic lattices made of triangular rods," Phys. Rev. B **97**(4), 045422 (2018).
13. A. B. Khanikaev, S. H. Mousavi, W. K. Tse, M. Kargarian, A. H. MacDonald, and G. Shvets, "Photonic topological insulators," Nat. Mater. **12**(3), 233–239 (2013).
14. L. H. Wu and X. Hu, "Scheme for achieving a topological photonic crystal by using dielectric material," Phys. Rev. Lett. **114**(22), 223901 (2015).
15. S. Barik, H. Miyake, W. DeGottardi, E. Waks, and M. Hafezi, "Two-dimensionally confined topological edge states in photonic crystals," New J. Phys. **18**(11), 113013 (2016).
16. T. Ma and G. Shvets, "All-Si valley-Hall photonic topological insulator," New J. Phys. **18**(2), 025012 (2016).
17. X. D. Chen, F. L. Zhao, M. Chen, and J. W. Dong, "Valley-contrasting physics in all-dielectric photonic crystals: orbital angular momentum and topological propagation," Phys. Rev. B **96**(2), 020202 (2017).
18. J. W. Dong, X. D. Chen, H. Zhu, Y. Wang, and X. Zhang, "Valley photonic crystals for control of spin and topology," Nat. Mater. **16**(3), 298–302 (2017).
19. X. Wu, Y. Meng, J. Tian, Y. Huang, H. Xiang, D. Han, and W. Wen, "Direct observation of valley-polarized topological edge states in designer surface plasmon crystals," Nat. Commun. **8**(1), 1304 (2017).
20. B. Hu, Q. J. Wang, and Y. Zhang, "Broadly tunable one-way terahertz plasmonic waveguide based on nonreciprocal surface magneto plasmons," Opt. Lett. **37**(11), 1895–1897 (2012).
21. F. Fan, S. Chen, X. H. Wang, and S. J. Chang, "Tunable nonreciprocal terahertz transmission and enhancement based on metal/magneto-optic plasmonic lens," Opt. Express **21**(7), 8614–8621 (2013).
22. L. Shen, Y. You, Z. Wang, and X. Deng, "Backscattering-immune one-way surface magnetoplasmons at terahertz frequencies," Opt. Express **23**(2), 950–962 (2015).
23. L. Shen, Z. Wang, X. Deng, J. J. Wu, and T. J. Yang, "Complete trapping of electromagnetic radiation using surface magnetoplasmons," Opt. Lett. **40**(8), 1853–1856 (2015).
24. F. Fan, C. Z. Xiong, J. R. Chen, and S. J. Chang, "Terahertz nonreciprocal isolator based on a magneto-optical microstructure at room temperature," Opt. Lett. **43**(4), 687–690 (2018).
25. B. Bahari, R. Tellezlimon, and B. Kanté, "Topological terahertz circuits using semiconductors," Appl. Phys. Lett. **109**(14), 143501 (2016).
26. L. He, Q. Shen, J. Xu, Y. You, T. Yu, L. Shen, and X. Deng, "One-way edge modes in a photonic crystal of semiconductor at terahertz frequencies," Sci. Rep. **8**(1), 8165 (2018).
27. J. Han, A. Lakhtakia, and C. W. Qiu, "Terahertz metamaterials with semiconductor split-ring resonators for magnetostatic tunability," Opt. Express **16**(19), 14390–14396 (2008).
28. J. Gómez Rivas, C. Janke, P. Bolivar, and H. Kurz, "Transmission of THz radiation through InSb gratings of subwavelength apertures," Opt. Express **13**(3), 847–859 (2005).
29. D. Xiao, M. C. Chang, and Q. Niu, "Berry phase effects on electronic properties," Rev. Mod. Phys. **82**(3), 1959–2007 (2010).
30. D. Jin, T. Christensen, M. Soljačić, N. X. Fang, L. Lu, and X. Zhang, "Infrared topological plasmons in graphene," Phys. Rev. Lett. **118**(24), 245301 (2017).

Optical Materials EXPRESS

31. T. Fukui, Y. Hatsugai, and H. Suzuki, "Chern numbers in a discretized Brillouin zone: efficient method to compute (spin) Hall conductances," J. Phys. Soc. Jpn. **74**(6), 1674–1677 (2005).